

Article

Uncovering *Streptomyces*-Derived Compounds as Cosmeceuticals for the Development of Improved Skin Photoprotection Products: An In Silico Approach to Explore Multi-Targeted Agents

Jeysson Sánchez-Suárez ^{1,2} , Luisa Villamil ¹ , Luis Díaz ^{1,2,*}  and Ericsson Coy-Barrera ^{3,*} ¹ Doctorate in Biosciences, School of Engineering, Universidad de La Sabana, Chía 250001, Colombia² Bioprospecting Research Group, School of Engineering, Universidad de La Sabana, Chía 250001, Colombia³ Bioorganic Chemistry Laboratory, Universidad Militar Nueva Granada, Cajicá 250247, Colombia

* Correspondence: luis.diaz1@unisabana.edu.co (L.D.); ericsson.coy@unimilitar.edu.co (E.C.-B.)

Abstract: The search for novel photoprotective substances has become a challenge in cosmeceutical research. *Streptomyces*-derived compounds can serve as a promising source of photoprotective agents to formulate skin photoprotection products, such as sunscreens. This study aimed to identify specialized metabolites with the potential to modulate UV-induced cellular damage in the skin by identifying potential multi-target-directed ligands. Using a combination of ligand- and target-based virtual screening approaches, a public compound library comprising 6524 *Streptomyces*-derived specialized metabolites was studied for their photoprotective capability. The compounds were initially filtered by safety features and then examined for their ability to interact with key targets in the photodamage pathway by molecular docking. A set of 50 commercially available UV filters was used as the benchmark. The protein–ligand stability of selected *Streptomyces*-derived compounds was also studied by molecular dynamics (MD) simulations. From the compound library, 1981 compounds were found to meet the safety criteria for topically applied products, such as low skin permeability and low or non-toxicity-alerting substructures. A total of 34 compounds had promising binding scores against crucial targets involved in UV-induced photodamage, such as serotonin-receptor subtype 5-HT_{2A}, platelet-activating factor receptor, IL-1 receptor type 1, epidermal growth factor receptor, and cyclooxygenase-2. Among these compounds, aspergilazine A and phaeochromycin F showed the highest ranked interactions with four of the five targets and triggered complex stabilization over time. Additionally, the predicted UV-absorbing profiles also suggest a UV-filtering effect. *Streptomyces* is an encouraging biological source of compounds for developing topical products. After in silico protein–ligand interactions, binding mode and stabilization of aspergilazine A and phaeochromycin F led to the discovery of potential candidates as photodamage multi-target inhibitors. Therefore, they can be further explored for the formulation of skin photoprotection products.

Keywords: sunscreen; photodamage; Actinobacteria; molecular docking; sunlight

Citation: Sánchez-Suárez, J.; Villamil, L.; Díaz, L.; Coy-Barrera, E. Uncovering *Streptomyces*-Derived Compounds as Cosmeceuticals for the Development of Improved Skin Photoprotection Products: An In Silico Approach to Explore Multi-Targeted Agents. *Sci. Pharm.* **2022**, *90*, 48. <https://doi.org/10.3390/scipharm90030048>

Academic Editor: William A. Donaldson

Received: 14 July 2022

Accepted: 5 August 2022

Published: 16 August 2022

Publisher's Note: MDPI stays neutral with regard to jurisdictional claims in published maps and institutional affiliations.



Copyright: © 2022 by the authors. Licensee MDPI, Basel, Switzerland. This article is an open access article distributed under the terms and conditions of the Creative Commons Attribution (CC BY) license (<https://creativecommons.org/licenses/by/4.0/>).

1. Introduction

Unprotected sun overexposure produces deleterious effects involving the detriment of cell membrane integrity and the induction of DNA damage, which can result in skin cancer [1,2]. The use of sunscreens is among the common photoprotection measures [3]; however, most of the sunscreens currently available focus on avoiding erythema but are ineffective against other photodamage outcomes such as oxidative stress and immunomodulation [4]. In addition to this limitation, several ultraviolet (UV) filters have claims for their safety (comprehensively reviewed by Paiva et al. [5]), ecotoxicity (aquatic ecosystem pollution) [6], marine life detriment [7–9], and bioaccumulation [10]. Under this scenario, research on new photoprotective agents is in high demand.

Sunlight irradiation is crucial for optimal health status. However, the portion of the spectrum below 400 nm (i.e., UV-B: 290–320 nm, and UV-A: 320–400 nm) can have acute and chronic harmful effects, most evident on the main exposed tissue, the skin. This UV-induced detrimental status is known as photoaging, and its development is mediated by several molecular mediators (previously reviewed by Poon et al. [11] and Bernard et al. [12]). This phenomenon has a clear immunomodulatory context involving numerous cytokines such as TNF- α , IL-1 α , IL-1 β , IL-4, IL-10, and PGE [11–16]. Intriguingly, the signaling pathways of many of these events include different membrane receptors found widely in keratinocytes and mast cells (Figure 1) [12–16]. This enables topical agents to block ligand binding with crucial receptors in photodamage molecular signaling, thereby producing a photoprotective effect. In contrast, most sunscreens comprise organic compounds that absorb UV radiation, and few incorporate bioactive agents that prevent the immunomodulatory signaling cascade.

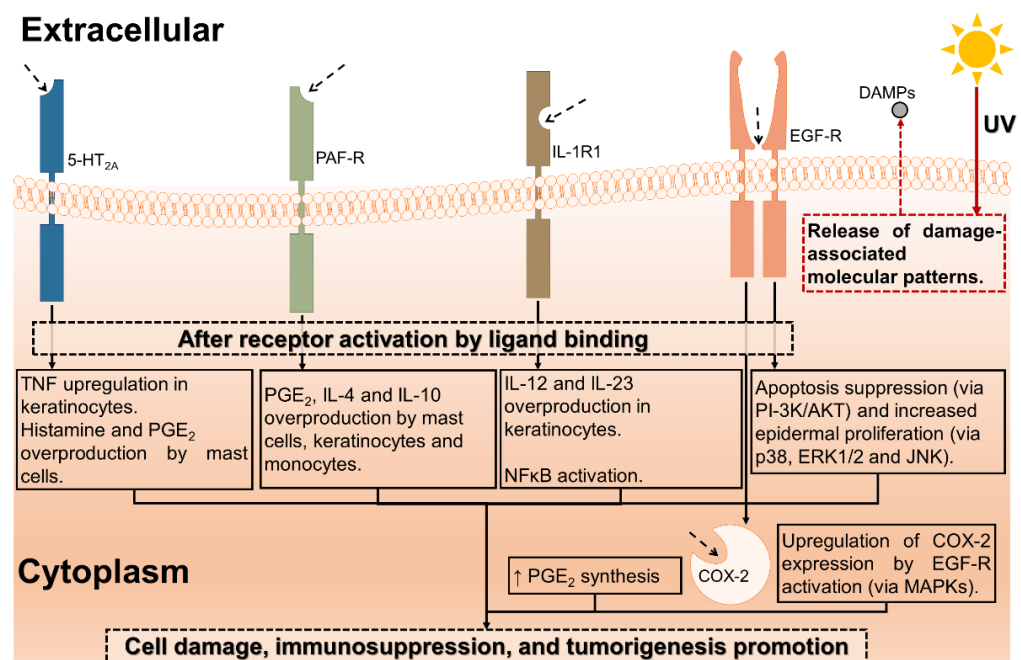


Figure 1. Schematic model of proteins involved in photodamage recognition and their inhibition sites. IL-1 receptor type I (IL-1R1), serotonin-receptor subtype 5-HT_{2A}, platelet-activating factor receptor (PAF-R), epidermal growth factor receptor (EGF-R), and cyclooxygenase-2 (COX-2) are crucial mediators in UV-induced carcinogenesis [12–16]. UV absorption by chromophores (e.g., *cis*-urocanic acid) induces the formation and release of damage-associated molecular patterns (DAMPs), which activate skin cell receptors with immunomodulatory effects (i.e., IL-1R1, 5-HT_{2A}, PAF-R, and EGF-R). Arrows indicate locations of the binding sites for each target.

An effective photoprotective agent hinders the photodamage mechanism by preventing oxidative stress and inflammation in addition to UV filtering [17,18]. However, most sun protection products employ UV filters as a functional ingredient [19,20], focusing on the mitigation of radiation while regardless of the control of cellular response, such as an increase in reactive oxygen intermediates and inflammatory response [21]. Currently, there is a claim to incorporate antioxidant agents into sunscreens [22]. Moreover, photoprotective agents must have low or no dermal bioavailability [23] to avoid side effects such as mutagenicity, hepatotoxicity, and endocrine disruption [24]. Such parameters should be taken into consideration when selecting active sunscreen ingredients.

Natural resources are an interesting and promising source of compounds possessing potent biological properties that have been traditionally exploited by the pharmaceutical industry [25]. The omics-based advances allowed the industry to overcome the main

constraints that usually challenge the development of products from naturally occurring compounds. Indeed, microbial-derived compounds offer a promising approach from applying culture media and metabolic and genetic engineering, among other alternatives [26]. Within the microorganism taxa, *Streptomyces* bacteria belonging to the Actinobacteria phylum provide a noteworthy model to search for biologically active metabolites, being the source of two-thirds of clinically employed antibiotics [27]. Furthermore, *Streptomyces*-derived metabolites with photoprotective potential have been recently reviewed [28], and compounds with antioxidant, anti-inflammatory, and UV-absorbing capacities were found. Although some compounds exhibited antioxidant and anti-inflammatory properties, no studies found three characteristics, as no photoprotective role was jointly observed. On the other hand, the chemo- and biodiversity shown by *Streptomyces*, along with the understanding about their culturing and metabolism regulation [27], led to the hypothesis that they can be considered as an encouraging resource of specialized metabolites with photoprotection-related activities. As this research can be highly expensive and time-consuming, computer-aided screening (i.e., in silico) is a valuable approach offering the opportunity to exploit large chemical libraries.

Various drugs have been discovered via in silico approaches [29], which have increasingly become important for drug design and development [30]. Virtual screening (VS) methods have demonstrated advantages over experimental high-throughput screening, such as in the fast and affordable discovery of lead and hit structures [31]. Additionally, the VS approach enables the study of compounds against targets whose experimental models do not exist. Another important advantage is the possibility of focusing on more than one biological target (multi-target drug discovery) [32], offering the potential to overcome some of the main limitations of the classical “one target, one drug” strategy [33]. Molecular docking (a three-dimensional [3D] target-based VS approach) [34] remains one of the most valuable drug discovery techniques over the past few years [35]. Once a suitable protocol is reached, predictions of ligand–target interactions can be accurately achieved by molecular docking [36,37], with the added benefit of being able to assess novel targets. Such ligand–target interactions through evaluation of the geometric properties of the simulated complex can be complemented by molecular dynamics (MD) simulations to explore information about binding mode and complex stabilization [38].

In this study, using a curated database with *Streptomyces*-derived compounds [39], we performed a computer-aided evaluation to disclose and identify photoprotective agents with improved safety and effectiveness features. Based on the protein structures available in the Protein Data Bank (PDB), we selected five crucial targets in the development of UV-induced damage (5-HT_{2A}, PAF-R, IL-1R1, EGF-R, and COX-2) [12,40]. Following a multi-target approach, we identified a group of compounds with promising docking scores with corresponding four out of the five screened targets. Additionally, MD simulations indicated that these compounds can stabilize the simulated complexes over time, involving various binding modes. Considering the role of these receptors in the signal transduction pathway of photodamage recognition, these compounds could act as potent photoprotective agents.

2. Materials and Methods

2.1. Ligand Selection and Preparation

The StreptomeDB 3.0 database, comprising 6524 compounds, was selected, as it provides a comprehensive repository of manually curated *Streptomyces*-derived metabolites [39]. The compound SMILES was collected from this database and entered into Osiris DataWarrior v5.5.0 [41] to calculate physicochemical properties and toxicological profiles. The compounds were filtered as follows: (1) according to their skin permeability potential and (2) their toxicological risk potential. The filtered compounds were then clustered by similarity based on the *Flexophore* descriptor in the DataWarrior v5.5.0 software. A representative molecule from each cluster was chosen for 3D sketching and optimization.

2.2. Protein Selection and Preparation

Five proteins involved in UV-induced skin damage were selected [12,40]; namely, platelet-activating factor receptor (PAF-R; PDB ID: 5ZKP), 5-hydroxytryptamine receptor 2A (5-HT_{2A}; PDB ID: 6A94), interleukin-1 receptor type 1 (IL-1R1; PDB ID: 4GAF), epidermal growth factor receptor (EGF-R; PDB ID: 4UV7), and prostaglandin G/H synthase 2 (COX-2; PDB ID: 5F1A). The X-ray crystallographic structures of these proteins were searched in the PDB using the coding gene names. The canonical sequences and topology descriptions were considered for selecting protein structure entry (information was obtained from the Universal Protein Resource) (UniProt, <https://www.uniprot.org/> (accessed on 12 July 2022)). Entries with the highest identity to the native protein with the best resolution were selected for molecular docking analysis.

2.3. Molecular Docking Studies

Target-based virtual screening was performed using AutoDock tools and the Vina plug-in [42]. Binding scores were calculated on a computer running Ubuntu 20.04.2 LTS 64-bit equipped with an Intel®Core™i7-4702MQ processor CPU @ 2.2 GHz (8 CPU) and 8 GB DDR3 RAM. According to each target's biochemical features, the grid box was defined as follows: PAF-R, 5-HT_{2A}, and COX-2 proteins with well-documented inhibition sites. Therefore, co-crystallized ligands were used for the grid box coordinate definition. For IL-1R1 and EGF-R, the grid box was specified based on their protein–protein interaction hot spots, whose inhibition capability has been previously described [43,44]. Thus, for IL-1R1, the grid box was defined on Arg271, Arg272, Glu202, Glu171, and Val117 residues [43], while the EGF-R grid box was defined on Tyr246/Tyr251 residues [44]. The coordinates of the grids used for each target were as follows: 5ZKP = 33.962, −5.769, and 9.629; 6A94 = 16.258, −0.380, and 56.903; 4GAF = −21.570, −35.710, and 21.150; 4UV7 = −40.725, −15.276, and 7.992; and 5F1A = 41.800, 24.200, and 240.100. Each cubic box was set to 25 × 25 × 25 number of points (npts) with 0.375 Å spacing. Three-dimensional visualization of the selected protein–ligand complexes' docking sites was performed in Discovery Studio Visualizer v21.1.0.20298 (BIOVIA, San Diego, CA, USA).

2.4. Quantum Properties of Top-Ranked Compounds and Theoretical Predictions of UV Spectra of A1 and A3

The SMILES of the top-ranked *Streptomyces*-derived compounds (n = 34) were transformed into 3D structures and compiled into an sdf file using Standardizer 19.21.0, 2019, ChemAxon (<http://www.chemaxon.com>; accessed on 2 April 2021). A Monte Carlo randomized conformational search was then performed, without any geometrical restrictions, using the semi-empirical AM1 parameterization using Spartan'14 (Wavefunction, Irvine, CA, USA) with a limit of 500 conformers. Energetically lowest stable conformers, within a 5 kcal/mol energy range, were geometrically optimized at the density functional theory (DFT) level using the B3LYP hybrid functional and 6-31+G (d,p) basis set using the Gaussian 09 program (Gaussian Inc., Wallingford, CT, USA). After structural optimization, harmonic vibrational frequencies were calculated at the same level of theory to verify the reliability of the stationary point at a minimum. All structures were converged successfully. The number of imaginary frequencies was zero for all the stationary points. During geometry optimization, the highest energy occupied molecular orbital (HOMO) and lowest energy unoccupied molecular orbital (LUMO) were also computed for further analysis. In addition, UV–Vis absorption spectra were also simulated for aspergilazine A (A1) and phaeochromycin F (A3) (disclosing allowed electronic transitions with wavelength and intensity) using time-dependent DFT formalism within the linear response regime using B3LYP functional with the 6-31+G (d) basis set. The polarizable conductor calculation model (CPCM) of solvation was employed for all calculations using water ($\epsilon = 78.36$) as solvent [45]. The theoretical absorption was normalized for comparative purposes.

2.5. Molecular Dynamics Simulations

MD simulations were conducted for the two top-ranked, best-docked compounds (A1 and A3; see Table 1) to explore the performance over time of these ligands within the binding sites of four targets (PAF-R, 5-HT_{2A}, IL-1R1, and EGF-R), using the YASARA v19.12.14 program (Biosciences GmbH, Vienna, Austria) [46] on Win10 and Dell Workstation. MD simulations were carried out using the AMBER14 force field in an explicit water environment and under constant pressure, periodic cell boundary condition, and 310 K. The solvated structure was minimized using the steepest descent method for 5000 steps at a temperature of 295 K and constant pressure. The simple point charge (SPC) water model was then implemented for solvation in a triclinic box using a 1.0 nm margin distance. Thereafter, 0.10 M NaCl was added to the simulation systems, and the water molecules were randomly replaced until neutrality. NVT (constant volume and temperature) equilibration at 310 K for 500 ps, followed by NPT (constant pressure and temperature) equilibration for 2000 ps using the Parrinello-Rahman method at 1 bar as a reference, were performed on the systems using position restraints. After equilibration, a production MD was run for 50 ns at a constant temperature (310 K) and pressure (1 bar). The coordinates were recorded every 10 ps. The electrostatic forces were calculated using the particle-mesh Ewald (PME) method. Periodic boundary conditions were used in all simulations, and covalent bond lengths were constrained by the linear constraint solver (LINCS) algorithm. The root mean square deviation (RMSD), root mean square fluctuation (RMSF), and radius of gyration (RoG) were analyzed for MD simulations. In addition, the binding free energy (BFE) was calculated using the g_mmpbsa tool [47]. These BFE calculations were performed for 60 snapshots taken at intervals of 500 ps during the last stable 30 ns MD simulations.

Table 1. Molecular docking results of Group A compounds.

Ligand	5-HT _{2A} BS ^a	RSD ^b	IL-1R1 BS ^a	RSD ^b	PAF-R BS ^a	RSD ^b	EGF-R BS ^a	RSD ^b
A1	-11.49 ± 0.03	0.28	-8.88 ± 0.28	3.13	-12.20 ± 0.00	0.00	-8.50 ± 0.00	0.00
A2	-5.50 ± 0.00	0.00	-9.10 ± 0.00	0.00	-12.40 ± 0.05	0.38	-9.14 ± 0.13	1.38
A3	-11.30 ± 0.00	0.00	-7.91 ± 0.03	0.40	-11.46 ± 0.05	0.45	-8.40 ± 0.00	0.00

^a BS = Binding scores as Vina outcome in kcal/mol. ^b Relative standard deviation, calculated from 10 independent docking runs.

2.6. Data Exploration and Statistical Analysis

Frequency distribution, mean, standard deviation, and relative standard deviation were used to describe the data. A Venn diagram was generated using the web-based tool InteractiVenn [48] to analyze the logical relationship between the hits found for each target (i.e., dataset). Inferential statistical analyses included the assessment of independence and normality distribution and homoscedasticity assumptions before each analysis. A descriptive summary of other results is presented. Receiver operating characteristic (ROC) curves were constructed, and the nonparametric Mann-Whitney *U* test was performed in GraphPad Prism v9.0.0 (GraphPad Software, San Diego, CA, USA). Differences were considered statistically significant at $p < 0.05$.

3. Results

3.1. Filtering of Streptomyces-Derived Compounds

To optimize the search for improved photoprotective agents in the StreptomeDB 3.0 database [39], we initially performed a selection based on skin permeability-related physicochemical properties. Percutaneous absorption is a decisive criterion for both the effectiveness and safety profile of photoprotective agents [49] and is related to physicochemical properties such as MW, melting point, H-donors, H-acceptors, cLogP, and cLogS [50]. Considering that the combination of MW, H-acceptors, cLogP, and cLogS works as a good predictor to classify the compound library into good and bad penetrants (i.e., “good penetrants” molecules with $MW \leq 152$, H-acceptors ≤ 3 , cLogP < 2.6 , and cLogS ≥ -2.3 ; “bad penetrants” molecules

with $MW > 213$, $H\text{-acceptors} \geq 3$, $cLogP > 1.2$, and $cLogS < -1.6$ [50]), these parameters were then calculated and used to filter the 6524 database compounds.

As a reference group, we selected 50 approved organic UV filters (AUVFs) [19,20]. From this group, we evaluated how AUVFs complied with the values as bad penetrants (i.e., with a poor dermal absorption capability). Remarkably, the AUVFs had the characteristics of bad penetrants. All of them met the criterion for at least one of the bad penetrant predictors (i.e., MW, H-acceptors, cLogP, and cLogS), while the majority (63.46%) fulfilled the criteria for four parameters (Figure 2a). According to this outcome, these parameters were also calculated for the whole StreptomeDB 3.0 library (Figure 2b). Thus, 3237 compounds (49.62%) were found to accomplish the criteria for four parameters (i.e., poorly penetrant compounds). The filtered compounds were examined for potential toxicity risk predictions to continue searching for enhanced prospects, such as mutagenicity, tumorigenicity, and reproductive and irritant effects.

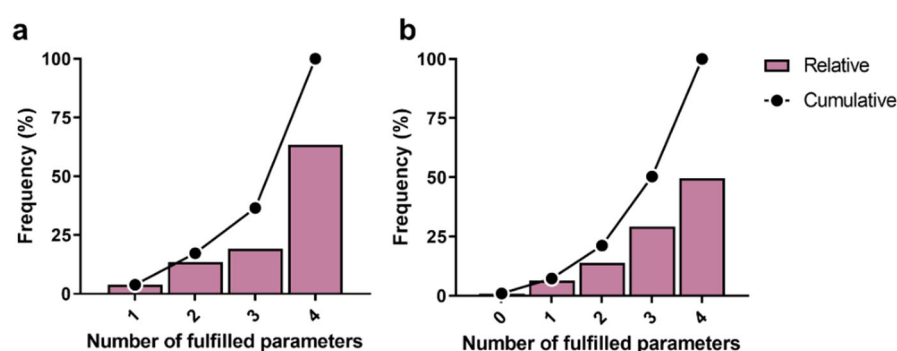


Figure 2. Skin permeability features of UV filters and *Streptomyces*-derived compounds. The MW, H-acceptors, cLogP, and cLogS parameters were calculated for the AUVFs ($n = 50$) and the *Streptomyces*-derived compounds ($n = 6524$). The compounds were classified according to the number of met parameters as bad penetrants (i.e., molecules with $MW > 213$, $H\text{-acceptors} \geq 3$, $cLogP > 1.2$, and/or $cLogS < -1.6$). In the plots, X-axis represents the number of parameters, and Y-axis represents the percentage frequency (bars to the relative frequency and dots to the cumulative frequency). (a) Approved organic UV filters group; (b) StreptomeDB 3.0 database compounds.

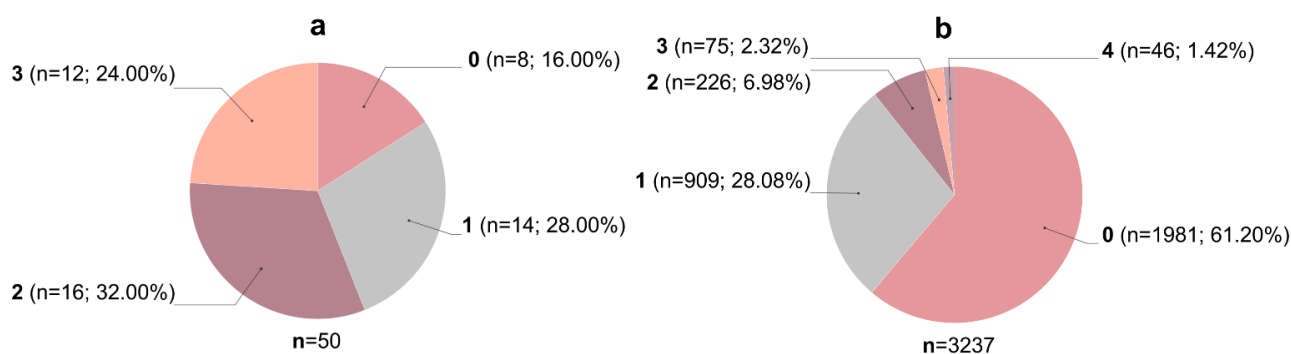


Figure 3. Toxicological profile of UV filters and *Streptomyces*-derived compounds. Toxicological effects such as irritant, mutagenic, tumorigenic, and reproductive effects were predicted using Datawarrior v5.5.0 software. The compounds were classified into group 0 (with “low” or “none” risk in the four parameters), group 1 (with “high” risk in at least one parameter), group 2 (with “high” risk in at least two parameters), group 3 (with “high” risk in at least three parameters), and group 4 (with “high” risk in the four parameters). (a) Approved organic UV filters; (b) filtered bad penetrants from *Streptomyces*-derived compounds.

For the 3237 selected compounds, potential toxicity risks were also predicted using DataWarrior v5.5.0 software (Figure 3, AUVFs provided a basis for comparison). DataWarrior classifies the risk into “high,” “low,” and “none” risks. As a result, 1981 (61.20%)

were predicted as “low” or “none” risk, contrasting with the 16.00% shown by AUVFs (Figure 3a). This low proportion of innocuousness in AUVFs is consistent with their current safety concerns [5]. This explores a possibility to find fewer toxic substances in the selected *Streptomyces*-derived compounds.

To continue filtering the chemical library, considering the likelihood of compounds with similar molecular-binding behavior, we analyzed the 3D-pharmacophore similarities within the double-filtered 1981 compounds using the *Flexophore* descriptor in DataWarrior [41]. This evaluation enabled the identification of 931 clusters with a unique ligand–protein interaction profile. The cluster size varied from 1 to 40 members; however, most (565; 57.59%) were single-member clusters (Table S1). A representative compound from each cluster was used for target-based virtual screening against PAF-R, 5-HT_{2A}, IL-1R1, EGF-R, and COX-2 (proteins involved in UV-induced skin damage [12,40]).

3.2. Molecular Docking Studies: Target-Based Virtual Screening

Molecular insights into the mechanisms of UV-induced deleterious effects have enabled the exploration of photoprotective strategies based on the search for inhibitors of crucial “targets” involved in skin photodamage/photoaging. Herein, we conducted target-based VS by molecular docking using the PDB structures of PAF-R, 5-HT_{2A}, IL-1R1, EGF-R, and COX-2 as targets. The co-crystallized ligands for PAF-R, 5-HT_{2A}, and COX-2 were re-docked to validate the docking protocol. Comparing the poses of the re-docking exercise with the experimental co-crystallized binding poses, the RMSD calculated were lower than 1.5 Å (Figure 4), indicating that the docking protocol could closely reproduce those binding poses [51]. In addition, a benchmarking approach was also used to assess the docking performance from the binding score results of the experimentally evaluated inhibitors in comparison to those of a group of inactive compounds (Figure 4d–f). The area under the curve (AUC) values of ROC curves were moderately well-fitted (>0.70), demonstrating that docking could discriminate between active and inactive compounds [51]. Unfortunately, these validations could not be performed for IL-1R1 and EGF-R because no experimental data involving the binding sites explored here were available.

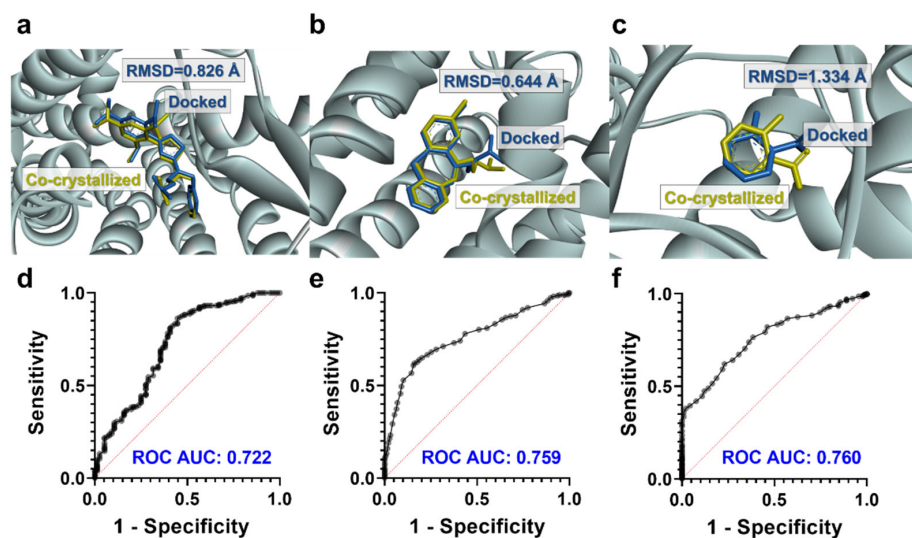


Figure 4. Docking protocol performance from experimentally evaluated ligands. The upper panels show the cartoon ribbon models with the co-crystallized ligands (yellow) and the re-docked ligands (blue) accompanied by the RMSD value. (a) Foropafant bound to PAF-R (PDB file: 5ZKP). (b) Zotepine bound to 5-HT_{2A} receptor (PDB file: 6A94). (c) Salicylate bound to COX-2 (PDB file: 5F1A). The lower panels show the receiver operating characteristic (ROC) curves based on data obtained by a benchmarking analysis of active and inactive ligands. (d) Ligands against PAF-R (n = 351, $p < 0.0001$). (e) Ligands against 5-HT_{2A} receptor (n = 449, $p < 0.0001$); (f) Ligands against COX-2 (n = 665, $p < 0.0001$).

Once the docking protocol was validated, the 931 representative compounds (defined by the *Flexphore* descriptor) were evaluated for in silico prediction of putative competitors. The binding scores varied for all targets. To select the compounds with the highest affinities, we analyzed the distribution of the binding scores by histograms for each target (Figure 5). Compounds within the lower 5th percentile were considered to have the best binding scores.

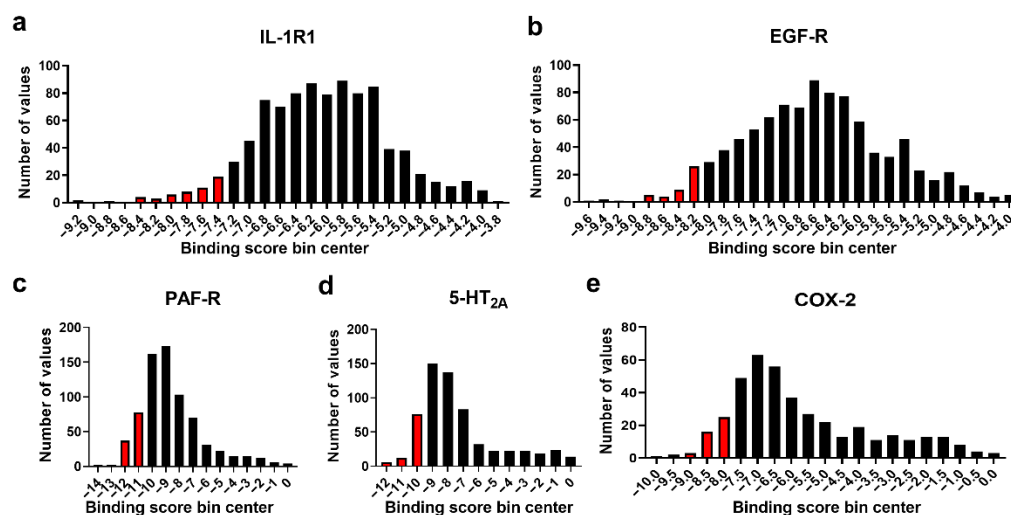


Figure 5. Results of the target-based virtual screening. Histograms analyzed the frequency distribution of the binding scores for each target. The X-axis represents the bin center of the binding score ranges, and the Y-axis represents the number of values. Red bars indicate values with the lower 5th percentile. Molecular docking results for (a) IL-1R1; (b) EGF-R; (c) PAF-R; (d) 5-HT_{2A}; (e) COX-2.

3.3. Identification of Multi-Target Ligands

Multi-target compounds were screened by drawing a Venn diagram with the molecules showing the best binding scores for each target (Figure 6). No compounds showed a high affinity for the five targets (i.e., zero at the intersection formed with the five targets).

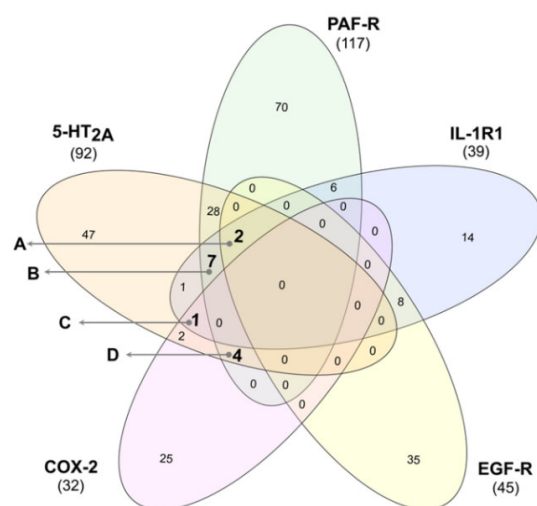


Figure 6. Multi-target representative compounds identified in the virtual screening. The compounds showing the best binding scores for each target were selected. The common compounds among the targets were identified using a five-way Venn diagram. The number of compounds selected for each group are in parentheses after oval shape headings. Common metabolites for at least three targets were defined as multi-target compounds. We found 14 multi-target representative compounds based on the intersects: (A) 5-HT_{2A}, PAF-R, IL-1R1, and EGF-R; (B) 5-HT_{2A}, PAF-R, and IL-1R1; (C) 5-HT_{2A}, IL-1R1, and COX-2; (D) 5-HT_{2A}, PAF-R, and COX-2.

We also identified compounds found in the intersections involving at least three targets, suggesting a multi-target high affinity. These compounds were classified into four groups (one per intersect) according to the proteins against which they showed the highest affinity, as follows:

1. Intersect **A**: two compounds with high affinity for 5-HT_{2A}, PAF-R, IL-1R1, and EGF-R.
2. Intersect **B**: seven compounds with high affinity for 5-HT_{2A}, PAF-R, and IL-1R1.
3. Intersect **C**: a compound with high affinity for 5-HT_{2A}, IL-1R1, and COX-2.
4. Intersect **D**: four compounds with high affinity for 5-HT_{2A}, PAF-R, and COX-2.

Remarkably, 5-HT_{2A} receptor was a common target in each group. The identified compounds corresponded to representative compounds from the clustering obtained using the *Flexophore* descriptor. As these 14 compounds represented 34 different compounds (i.e., 14 representative and 20 unevaluated cluster members), a new docking evaluation was performed with all the clustered compounds.

Among the 34 compounds (Figure 7), seven were unique (i.e., the *Flexophore* descriptor did not find similarity with another compound, and they corresponded to **A3**, **B21**, **B22**, **B23**, **B24**, **D33**, and **D34**). In contrast, the remaining 27 compounds were grouped into seven clusters: (i) **A1–A2**, (ii) **B4–B8**, (iii) **B9–B13**, (iv) **B14–B20**, (v) **C25–C28**, (vi) **D29–D32**, and (vii) **D31–D32**. As expected, in most cases (90.48%), the compounds within each cluster displayed similar binding scores (Tables 1–4), supporting the usefulness of the *Flexophore* descriptor in filtering large chemical libraries to time and cost optimization in VS campaigns.

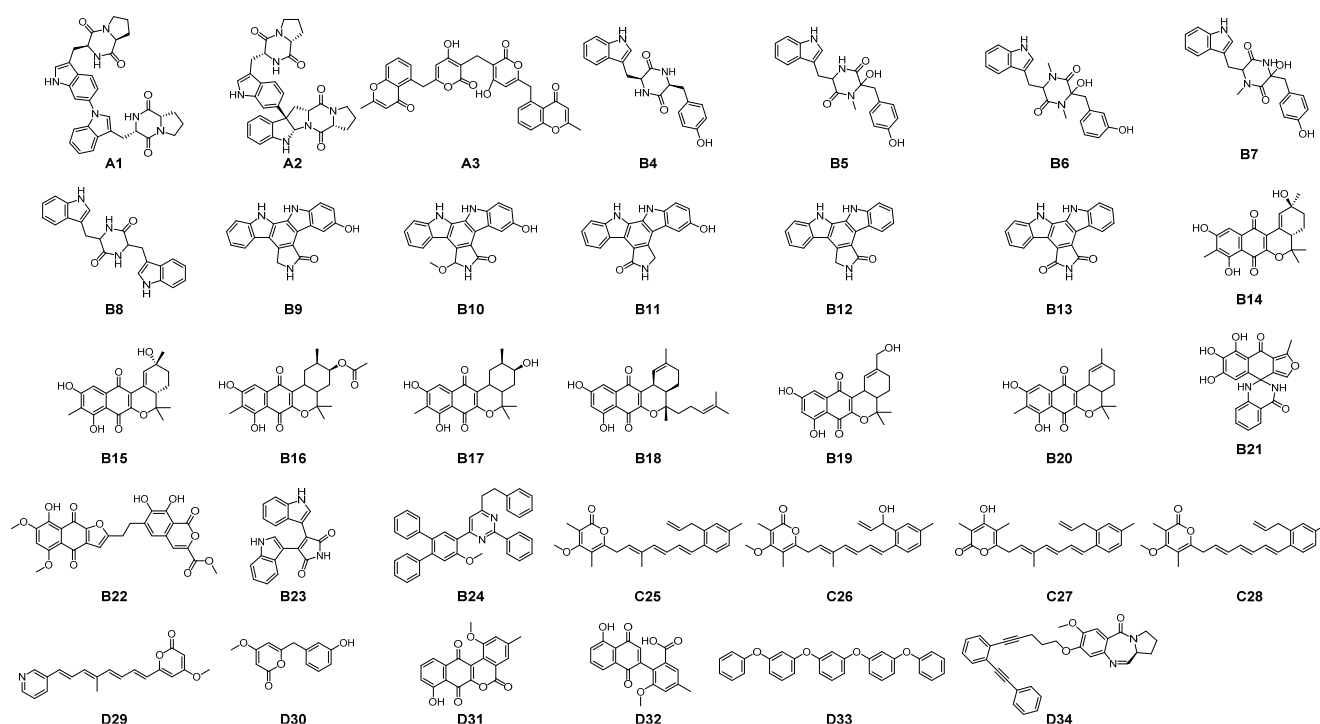


Figure 7. Chemical structures of the compounds with the best binding scores.

Table 2. Molecular docking results of Group B compounds.

Ligand	5-HT _{2A} BS ^a	RSD ^b	IL-1R1 BS ^a	RSD ^b	PAF-R BS ^a	RSD ^b
B4	-10.00 ± 0.00	0.00	-7.50 ± 0.00	0.00	-11.00 ± 0.00	0.00
B5	-9.90 ± 0.00	0.00	-7.81 ± 0.03	0.40	-10.30 ± 0.00	0.00
B6	-9.60 ± 0.00	0.00	-7.40 ± 0.00	0.00	-11.06 ± 0.05	0.47
B7	-9.61 ± 0.03	0.33	-7.00 ± 0.00	0.00	-10.50 ± 0.32	3.01
B8	-10.71 ± 0.03	0.30	-7.74 ± 0.21	2.67	-11.80 ± 0.00	0.00
B9	-10.51 ± 0.03	0.30	-7.60 ± 0.00	0.00	-11.70 ± 0.00	0.00
B10	-10.40 ± 0.00	0.00	-7.69 ± 0.03	0.41	-11.39 ± 0.03	0.28
B11	-10.80 ± 0.00	0.00	-7.51 ± 0.03	0.42	-11.41 ± 0.03	0.28
B12	-10.66 ± 0.05	0.48	-7.60 ± 0.00	0.00	-11.60 ± 0.00	0.00
B13	-10.53 ± 0.05	0.46	-7.80 ± 0.00	0.00	-12.10 ± 0.00	0.00
B14	-10.37 ± 0.41	3.96	-7.50 ± 0.00	0.00	-10.80 ± 0.00	0.00
B15	-8.71 ± 0.03	0.36	-7.18 ± 0.38	5.29	-10.40 ± 0.00	0.00
B16	-10.00 ± 0.00	0.00	-7.19 ± 0.37	5.10	-10.58 ± 0.04	0.40
B17	-9.70 ± 0.00	0.00	-7.23 ± 0.35	4.79	-10.10 ± 0.00	0.00
B18	-7.94 ± 0.18	2.24	-6.50 ± 0.17	2.61	-11.19 ± 0.03	0.28
B19	-8.36 ± 0.05	0.62	-6.85 ± 0.13	1.85	-10.00 ± 0.00	0.00
B20	-8.89 ± 0.03	0.36	-6.40 ± 0.00	0.00	-10.90 ± 0.00	0.00
B21	-10.50 ± 0.00	0.00	-7.59 ± 0.23	3.07	-11.00 ± 0.00	0.00
B22	-10.50 ± 0.00	0.00	-7.59 ± 0.06	0.75	-10.97 ± 0.05	0.44
B23	-10.10 ± 0.00	0.00	-7.69 ± 0.03	0.41	-10.80 ± 0.00	0.00
B24	-11.91 ± 0.03	0.27	-7.38 ± 0.04	0.57	-13.91 ± 0.03	0.23

^a BS = Binding scores as Vina outcome in kcal/mol. ^b Relative standard deviation, calculated from 10 independent docking runs.

Table 3. Molecular docking results of Group C compounds.

Ligand	5-HT _{2A} BS ^a	RSD ^b	IL-1R1 BS ^a	RSD ^b	COX-2 BS ^a	RSD ^b
C25	-10.76 ± 0.07	0.65	-7.38 ± 0.04	0.57	-8.93 ± 0.05	0.54
C26	-10.77 ± 0.05	0.45	-7.42 ± 0.06	0.85	-8.63 ± 0.05	0.56
C27	-11.45 ± 0.05	0.46	-7.40 ± 0.00	0.00	-8.83 ± 0.05	0.55
C28	-10.64 ± 0.07	0.66	-7.19 ± 0.06	0.79	-8.43 ± 0.15	1.77

^a BS = Binding scores as Vina outcome in kcal/mol. ^b Relative standard deviation, calculated from 10 independent docking runs.

Table 4. Molecular docking results of Group D compounds.

Ligand	5-HT _{2A} BS ^a	RSD ^b	PAF-R BS ^a	RSD ^b	COX-2 BS ^a	RSD ^b
D29	-9.96 ± 0.05	0.52	-10.59 ± 0.03	0.30	-8.69 ± 0.03	0.36
D30	-8.20 ± 0.00	0.00	-8.52 ± 0.04	0.49	-7.80 ± 0.28	3.58
D31	-10.10 ± 0.00	0.00	-10.75 ± 0.05	0.49	-6.89 ± 1.80	26.06
D32	-8.81 ± 0.06	0.64	-9.90 ± 0.00	0.00	-6.01 ± 1.45	24.12
D33	-12.27 ± 0.05	0.39	-11.71 ± 0.03	0.27	-8.96 ± 0.05	0.58
D34	-11.59 ± 0.03	0.27	-11.64 ± 0.07	0.60	-9.16 ± 0.38	4.16

^a BS = Binding scores as Vina outcome in kcal/mol. ^b Relative standard deviation, calculated from 10 independent docking runs.

Although several compounds displayed encouraging binding scores (Tables 1–4), **A1** (aspergilazine A) and **A3** (phaeochromycin F) exhibited the highest affinities against the highest number of targets among the evaluated compounds (Table 1). The former is an indole/pyrazinedione-containing alkaloid, and the latter is a chromen-4-one/pyran-2-one-containing polyketide; both types have been previously described with photoprotection-related activities [28]. Based on these observations, the binding modes of these compounds were analyzed.

As several UV filters have been reported to have anti-inflammatory activity [52], we evaluated their behavior as ligands against the five targets (i.e., 5-HT_{2A}, PAF-R, IL-1R1, EGF-

For instance, although **A1** formed more conventional *H*-bonds with 5-HT_{2A} (residues Cys227, Phe234, and Ser242; Figure 9a) than with PAF-R (residues Tyr77, Tyr151, and Tyr177; Figure 9b), the *H*-bonds with PAF-R were stronger than those for 5-HT_{2A} (i.e., 2.56 ± 0.27 Å for PAF-R against 2.79 ± 0.48 Å for 5-HT_{2A}). Regarding IL-1R1 and EGF-R, the lower number of conventional *H*-bonds in EGF-R was compensated for by a higher number of hydrophobic interactions (Figure 9c,d). In the case of IL-1R1, **A1** formed conventional *H*-bonds with Asn204, Lys270, and Thr300. In addition, two non-conventional *H*-bonds also appeared to be involved: Gln236 with the indole moiety (two π -hydrogen bonds, Figure 9c) and one hydrophobic interaction between Lys270 and the second **A1** indole moiety. For EGF-R, the residues participating in the binding were Gly574 (through conventional *H*-bond), Thr239, Pro242, and Leu243 (these three by hydrophobic interactions), as shown in Figure 9d.

The binding modes of phaeochromycin F showed similar binding scores for 5-HT_{2A} and PAF-R and no differences between IL-1R1 and EGF-R (Table 1). Interestingly, **A3** showed a higher number of interactions with each target than **A1** (Figure 10), despite the similar affinities calculated for both compounds (Table 1). A cation- π electrostatic interaction between Arg271 and the **A3** 2*H*-pyran-2-one moiety (Figure 10c) could improve the binding mode and enhance the complex stability [53].

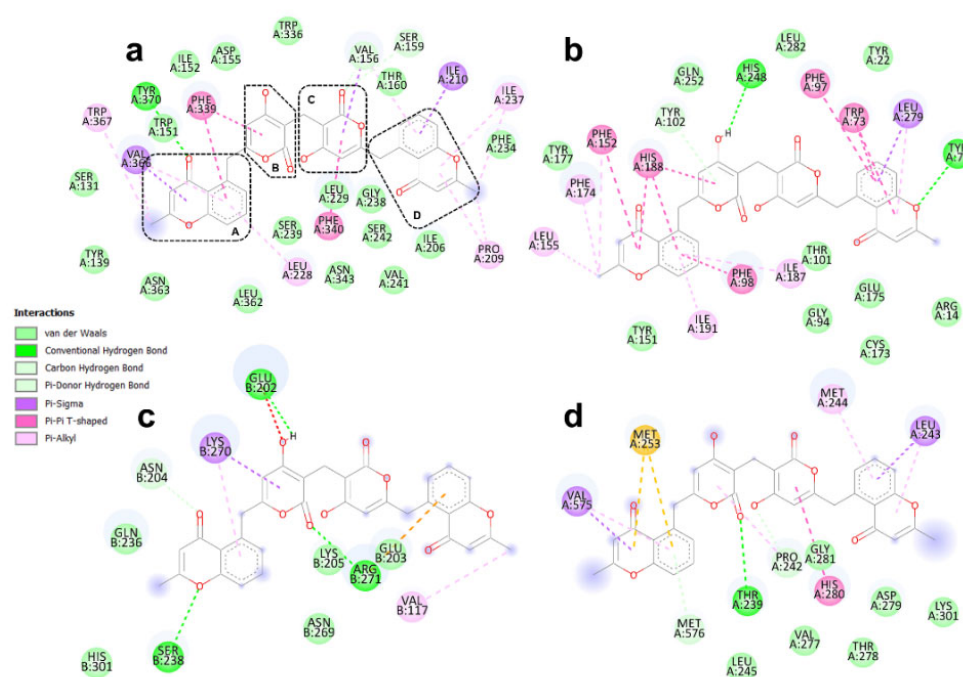


Figure 10. Receptor–ligand interactions of phaeochromycin F (**A3**). The interactions between phaeochromycin F and the residues involved in the binding sites for (a) 5-HT_{2A}; (b) PAF-R; (c) IL-1R1; (d) EGF-R are shown. In (a), the phaeochromycin F substructures are indicated as follows: A and D represent the 4*H*-chromen-4-one moiety; B and C represent the 2*H*-pyran-2-one moiety. The color legend indicates the type of interaction. Green colors represent *H*-bond-type interactions, and pink–purple colors are used for hydrophobic interactions. In IL-1R1 (c), yellow color indicates cation- π electrostatic interaction. In EGF-R (d), yellow color indicates π -sulfur interaction.

3.5. Molecular Dynamics Simulations

We performed 50 ns MD simulations using target proteins alone and docked distinctly with compounds **A1** and **A3** to extend the information on the binding modes of these top-ranked, best-docked compounds. Ligand–protein trajectories of the resulting complexes were examined through the variation of geometric properties over time. Thus, the RMSD of the protein backbone reflected the receptor frame stability by computing the time-dependent distance (Å) among distinct positions of the atom set (Figure 11). In general, the protein alone exhibited a normal evolution during the simulation but showed

a slight perturbation at 10–20 ns (RMSD 1–6 Å). However, normal stabilization was reached throughout the remaining MD simulation (RMSD 3–12 Å). The most perturbed protein was IL-1R1, as it exhibited a high perturbation at 20 ns, involving an RMSD increase from 3 to 11 Å, but reached stability after 25 ns. For all four test protein–ligand complexes, compounds **A1** and **A3** promoted stability, as the RMSD values decreased substantially (between 1 and 6 Å) from 10 ns. Hence, compound **A1** stabilized the protein IL-1R1, whereas **A3** promoted stability in 5-HT_{2A} and EGF-R. Both test compounds exhibited similar behavior within the binding site of PAF-R. A steady simulation progress of the complex stability was retained over the remaining time for these two ligands (>30 ns). In addition, compound **A3** exhibited the least perturbed MD performance within the binding sites of EGF-R and 5-HT_{2A}, indicating good geometric properties that interact with these targets. In contrast, the most-perturbed MD behavior was observed for compounds **A1** and IL-1R1 between 12 and 25 ns; however, the complex evolved satisfactorily and reached stability above 30 ns. The computed variations in RMSD values for these complexes showed that the protein structures were differentially affected by the interaction with these two ligands but achieved stability at the end of each MD simulation.

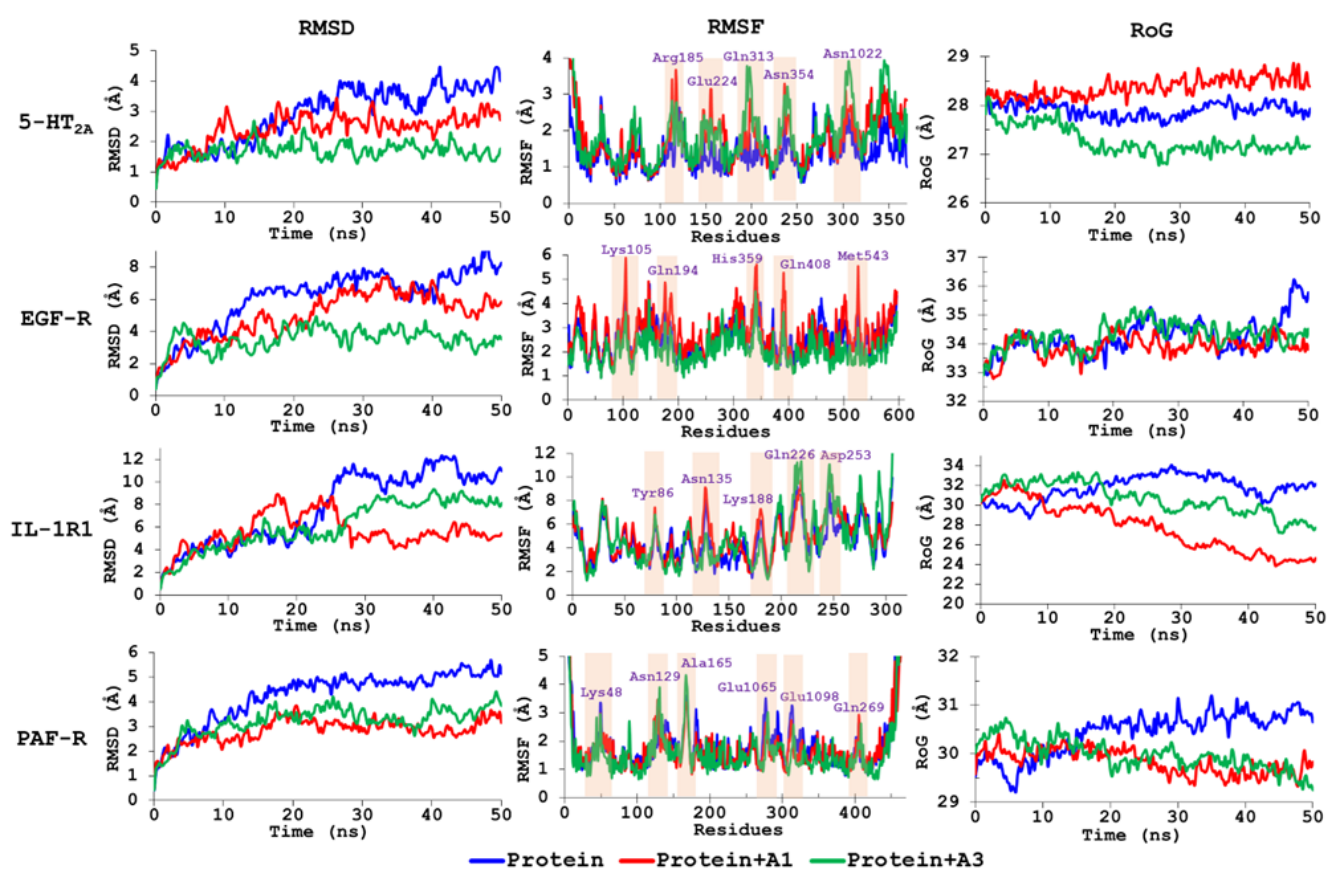


Figure 11. Molecular dynamics (MD) simulations during 50 ns for target proteins alone, i.e., 5-HT_{2A}, EGF-R, IL-1R1, and PAF-R (blue line) and docked separately with **A1** (red line), and **A3** (green line). First column: root mean square deviations (RMSD) along MD-simulated trajectories. Second column: root mean square fluctuations (RMSF) of protein residues along MD-simulated trajectories. Third column: radius of gyration (RoG) along MD-simulated trajectories.

Fluctuations in the C α atomic positions for each residue of the proteins were also explored using RMSF. The flexibility and secondary structure of the target proteins were examined when bound with compounds **A1** and **A3**. Constrained regions were found to have lower RMSF values, and higher RMSF values indicated more flexibility. MD-simulated protein–ligand pairs exhibited distinctive behavior (Figure 11), including fluctuations

ranging from 2 to 6 Å and comprising alterations near the previously mentioned crucial interactions from the docking simulations. Additionally, in comparison to the proteins alone, binding with the tested ligands **A1** and **A3** caused considerable variations in RMSF values. Except for Gln269 in PAF-R, the identified residues (Figure 11) were part of loops, indicating possible residues that served as pivotal parts of the proteins to partially modify the tertiary structure and promote ligand binding. Gln269 is located near helix VII of PAF-R. The influence of Gln residues on alpha helix stability has been shown to be position-dependent [54]. In addition, Gln residues can form hydrogen bonds with the side chains of neighboring residues that may be weak [55], in this case with Asp273, resulting in oscillations that change the contribution of these interactions to the α -helix stability.

The observed performance of the evolution of the packing levels of complexes during the simulation time from the information of the RoG was found to be different (Figure 11). The **A1**- and **A3**-EGF-R complexes were found to be similar to those of the receptor alone; therefore, receptor packing can be considered unaffected by these interactions. In contrast, the complexes formed by the two ligands and PAF-R and IL-1R1 promoted a higher protein deformation, involving a reduction in the overall compactness (typically for α/β -proteins) that would lead to the inactivation of the respective proteins. Finally, compounds **A1** and **A3** exhibited the opposite behavior of interacting with 5-HT_{2A} protein, as **A1** promoted an increase in the packing level of this protein (*ca.* 1 Å), whereas **A3** favored a reduction in its compactness (*ca.* 2 Å). Although the protein–ligand interactions can affect the 3D-packing of the test complexes, a reasonably steady folding reflects their stability after binding between target proteins and test compounds.

The BFEs (ΔG_{bind}) for the best-docked compounds (i.e., **A1** and **A3**) during the interaction of target proteins for the last 30 ns of the MD trajectory were estimated using the MM/PBSA approach to evaluate the global stability of the resulting ligand–enzyme complexes. The calculated binding energies are presented in Table 5. The most negative ΔG_{bind} resulted in the IL-1R1-**A1** complex (i.e., -206.1 kJ/mol). The two test ligands exhibited negative binding energies, and differences between the ligands were observed, which explains the resulting docking performance. The major contribution to the binding energy was due to van der Waals (ΔE_{vdW}) energies (< -140 kJ/mol), which resulted in comparable values among the test compounds, while the contribution of electrostatic energy exhibited higher differences between them. Compound **A3** exhibited the lowest electrostatic energy for all protein targets, whereas **A1** exhibited the highest electrostatic energy. In addition, the contribution of polar solvation energy was found to be more unfavorable for both ligands. The solvent-accessible surface area (SASA) energy was similar for the test ligands, even though compound **A3** generally exhibited the highest ΔG_{sasa} . Therefore, according to these results, electrostatic and polar solvation energy contributions could rationalize the difference in the binding modes of the test ligands, which showed an important role of hydrophobic interactions in the stabilization and even binding of test compounds within the inhibition sites of the target proteins. Consequently, non-polar electrostatic interactions could be implied as the main driving force for the molecular recognition of these four targets by compounds **A1** and **A3**.

Table 5. Binding-free and related energies (kJ/mol) calculated by the molecular mechanics/Poisson–Boltzmann surface area (MM/PBSA) method for the top-ranked, best-docked compounds within the binding sites of four protein targets.

Ligands	Targets	ΔE_{vdW}^a	ΔE_{ele}^b	ΔG_{sol}^c	ΔG_{sasa}^d	ΔG_{bind}^e
A1	5-HT _{2A}	-164.5 ± 1.8	-139.4 ± 1.9	207.8 ± 1.5	-22.3 ± 2.2	-118.4 ± 1.9
	EGF–R	-141.8 ± 2.6	-128.6 ± 1.7	187.6 ± 2.6	-19.6 ± 2.3	-102.4 ± 2.3
	IL–1R1	-207.7 ± 2.1	-121.4 ± 2.2	144.3 ± 1.2	-21.3 ± 2.4	-206.1 ± 1.7
	PAF–R	-216.9 ± 3.2	-138.6 ± 2.4	208.6 ± 3.5	-20.9 ± 2.1	-167.8 ± 2.8
A3	5-HT _{2A}	-211.8 ± 3.5	-105.3 ± 1.9	180.3 ± 2.8	-23.6 ± 2.0	-160.4 ± 2.5
	EGF–R	-215.8 ± 3.4	-112.5 ± 2.6	194.3 ± 2.4	-24.1 ± 1.8	-158.1 ± 2.7
	IL–1R1	-198.6 ± 2.8	-109.7 ± 2.5	186.5 ± 2.9	-23.9 ± 1.6	-145.7 ± 2.4
	PAF–R	-216.4 ± 1.9	-111.2 ± 0.8	185.1 ± 3.1	-21.4 ± 1.1	-163.9 ± 1.9

^a van der Waals energy; ^b electrostatic energy; ^c polar solvation energy; ^d solvent accessible surface area (SASA) energy; ^e binding free energy. Energies are expressed as mean values (in kJ/mol) \pm standard deviations.

3.6. UV-Absorbing Profile of the Selected Multi-Target Compounds

We have outlined *Streptomyces*-derived compounds with the potential to serve as blockers of critical targets in photodamage signaling. However, the quality of UV radiation absorption is present in most organic compounds, and it could enhance the photoprotective features of the identified compounds. Therefore, the HOMO–LUMO transitions of the 34 selected compounds were calculated. These calculations were also performed for AUVFs, as a reference group.

In organic compounds, such as AUVFs, the mechanism of UV radiation absorption is explained by electronic transitions, particularly of π -conjugated systems [19]. This is consistent with the frequency distribution of the calculated HOMO–LUMO gaps, with values of 391.8, 415.6, and 449.6 kJ/mol, for the 25th, 50th, and 75th percentiles, respectively. Most of the data were clustered between these percentiles, which can be evidenced by the constricted size of the box in Figure 12a (UV filters). In the case of *Streptomyces*-derived compounds, the values of the HOMO–LUMO gaps had a wider dispersion and differed significantly ($p = 0.0082$) from those of AUVFs (Figure 12a). However, several compounds (including A1 and A3) had similar values to those of AUVFs, suggesting an electronic transition similar to that exhibited by UV filters. This finding led us to explore the UV absorption profiles of A1 and A3.

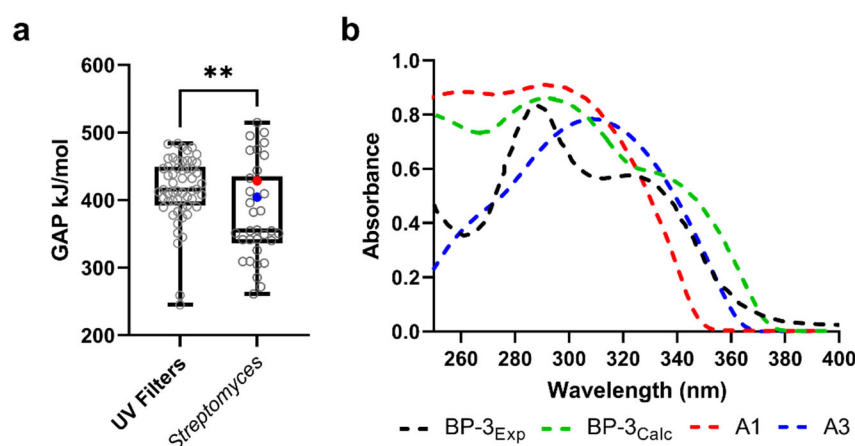


Figure 12. UV-absorbing profile of the selected *Streptomyces*-derived compounds. (a) Comparison between HOMO–LUMO gaps of AUVFs and selected *Streptomyces*-derived compounds. Red and blue dots are related to the energy gaps of A1 and A3, respectively. The nonparametric Mann–Whitney U test was used to evaluate the significant difference between the groups; ** p -value = 0.0082. (b) Experimental UV spectrum of oxybenzone is compared with the calculated spectra of oxybenzone, A1 and A3.

To validate the theoretical data, we compared the experimental UV absorbance spectrum of oxybenzone (BP-3; one of the most used UV filters used in the manufacture of sunscreens [56]) with the *in silico* calculated UV spectra (Figure 12b). In the UV-B and UV-A range (i.e., 290–400 nm), the experimental and calculated BP-3 spectra were quite similar according to the critical wavelength (λ_C) and the UVA/UVB ratio calculated for each spectrum (λ_C and the UVA/UVB ratio are measures of UV-blocking capacity [57]). For instance, λ_C was 350 and 353 nm for the experimental and calculated UV spectra, respectively. Likewise, the UVA/UVB ratio was 0.93 and 0.94 for the experimental and calculated UV spectra, respectively.

Regarding the UV absorption profile for **A1** and **A3**, **A1** would absorb more in the UVB and UVA2 regions (i.e., 320 to 340 nm) with a λ_C of 340 nm and a UVA/UVB ratio of 0.68. **A3** exhibited a better UV-absorbing capacity for UVA1 (340–400 nm) with a λ_C of 351 nm and a UVA/UVB ratio of 1.31. These data provide an idea about the capability of these compounds to behave as UV filters, enhancing their properties as photoprotective agents.

4. Discussion

In silico approaches have played a significant role in the identification of candidate compounds for the development of products to control detrimental processes [58]. Among the various benefits of computer-aided techniques, it is worth highlighting the evaluation of a large compound dataset with an excellent cost-effectiveness balance [30], limited use of animal models [30], and rationalizing raw materials, to act as a crucial factor in lead and hit discovery from natural products [59]. Herein, we report naturally occurring compounds that can serve as lead or reference skeletons for the development of novel photoaging and photocarcinogenesis control agents by combining ligand-based and structure-based approaches.

Photoaging is a condition that affects the cosmetic aspect of the skin and its physiological roles, namely, immunomodulatory effects [11]. Although several molecular mechanisms that mediate the response to actinic damage have been described, most photoprotective products lack antagonistic action targeting photodamage mediators, such as reactive oxygen species (ROS) and proinflammatory cytokines. Several mediators initiate an immunomodulatory effect on various cells during an early photodamage event in the skin. The availability of identified and characterized photodamage-related targets opens a promising opportunity to explore novel photoprotection strategies using small molecule antagonists [12,60,61]. Here, we identified 34 *Streptomyces*-derived compounds that showed promising docking scores against the targets evaluated here (i.e., 5-HT_{2A}, PAF-R, IL-1R1, EGF-R, and COX-2). Several of these molecules have been described as antimicrobial and antitumor compounds (e.g., **B11**, **B12**, **B13**, and **D34**). However, compounds such as **A2** [62], **A3** [63], **B10** [64], and **D30** [65] have shown weak or no cytotoxic activity, which is a critical factor in the search for topically applied products for skincare. This, coupled with the potential to interact simultaneously with different targets, makes these promising compounds for the development of skincare products. Particularly, **A1** and **A3** were the compounds with best-docking scores and involved the highest number of targets (4 out of 5); namely, 5-HT_{2A}, PAF-R, IL-1R1, and EGF-R.

As skin photocarcinogenesis follows a multi-step model [66], preventive strategies should also reflect a multi-target approach. In this scenario, compounds such as **A1** and **A3** showed feasible binding modes against several photodamage targets. Interestingly, although both compounds are structurally different, both **A1** and **A3** are asymmetric dimers. The former is a diketopiperazine, while the latter is a polyketide with 4*H*-chromen-4-one and 2*H*-pyran-2-one moieties. The anti-inflammatory potential of diketopiperazine-type compounds has been previously reported [67,68]. In these reports, diketopiperazines inhibited TNF- α release by cells pulsed with lipopolysaccharide (LPS). Remarkably, LPS-induced TNF release has been found to be PAF-dependent both in *in vitro* [69] and *in vivo* [70] models. These findings demonstrate the significance and plausibility of inflammation control mediated by the inhibition of surface receptors such as PAF-R. The anti-inflammatory

potential of compounds with 4*H*-chromen-4-one moieties has also been demonstrated [71], including in phaeochromycin-like molecules [72].

Promiscuous compounds, interacting with more than one target, have been shown to offer advantages over the classical one-target compounds [33]. Here, the binding modes shown by **A1** and **A3** involved crucial sites within all membrane surface receptors tested. For instance, **A1** interacted with Val156, Leu229, Trp336, Phe339, and Phe340 residues on 5-HT_{2A} (Figure 9a), which are also involved in zotepine interactions (a 5-HT_{2A} approved antagonist) [73]. Similarly, **A3** interactions involve crucial residues (i.e., Val156, Ser159, Phe339, and Phe340, Figure 10a) for inhibitory actions on 5-HT_{2A} [73]. Unlike 5-HT_{2A} and PAF-R, in the molecular pathways of IL-1 α / β and EGF-R, their activation involves a protein–protein interaction (PPI) mechanism [13,74]. Although this scenario is more complex than inhibiting protein–ligand interactions, blocking the hotspots in PPIs is a promising mechanism to block a detrimental signaling pathway [75]. **A1** and **A3** displayed a potential blocking binding mode on the PPI hotspots for IL-1R1 and EGF-R.

For IL-1R1, **A3** presented a more likely blocking effect than **A1**, considering the interaction with the hot spots Arg271 and Val117 [43]. However, **A1** interacted with nearby hot spot residues, such as Lys270 and Asn204. Indeed, residues Gln236 and Asn204 have been reported to impact the IL-1 α /IL-1R1 interaction [76], contributing to the inhibition of IL-1 signaling. In the EGF-R case, homodimerization is a crucial step for activation and signaling [74]. It has been reported that residues 242–259 conform to a critical region in the EGF-R dimer interface [44,77]. Mutagenesis assays have supported the significance of these residues in the dimerization and activation of EGF-R [77,78]. Blocking these hot spots with NSC56452 (a small molecule) inhibited EGF-R activation [44]. Although **A1** and **A3** did not interact with the most critical residues (i.e., Tyr246 and Tyr251), their interactions involved several nearby residues (Figures 9d and 10d). In fact, **A3** displayed interaction with various residues of the dimerization arm, such as Pro242, Leu243, Met244, and Met 253 (Figure 10d).

Considering the MD results, we hypothesized that the combination of **A1** and **A3** could ensure a potent inhibitory effect. For IL-1R1, the most stable complex was formed with **A1**, as explained by the calculations shown in RMSD, RoG, and ΔG_{bind} (Figure 11 and Table 5). For 5-HT_{2A}, the binding to **A3** was very stable, even improving the RMSD and RoG values shown by the apoprotein. Meanwhile, for EGF-R and PAF-R, the complexes with both compounds were found to be comparable, except for ΔG_{bind} with EGF-R. The latter is explained by the differences between ΔE_{vdW} , which was more favorable for **A3**. Thus, each compound shows promising results that could lead to the development of inhibitors of distinct UV-induced detrimental signaling pathways.

Additionally, the UV-absorbing profile calculated for **A1** and **A3** (Figure 11) makes them ideal candidates for photoprotectants. The most striking is that the compounds could complement each other, absorbing UV-B and UV-A radiation. While the results allow us to postulate that **A1** has a higher UV-B and UV-AII absorption capacity, this could be compensated by the λ_C and UVA/UVB ratio calculated for **A3** (Figure 12b). Additionally, both compounds exhibited HOMO-LUMO gaps, similar to AUVFs (Figure 12a). Taken together, these results suggest that **A1** and **A3** could serve as multipurpose agents, not only reducing the molecular UV-induced response but also filtering some portion of the UV radiation. Furthermore, as the 34 compounds identified have π -conjugated systems (Figure 7), they represent attractive options for their UV-absorbing potential. This fact is of particular interest, considering the potential effect on the mitigation of tissue damage due to the inflammatory response.

Considering UV-induced signaling events, we hypothesize that **A1** and **A3** can exert a potent photoprotective effect mediated by the following mechanism of action (Figure 13):

- (i.) Mitigating the amount of radiation that would reach the cells by absorption.
- (ii.) Inhibiting 5-HT_{2A} activation triggered by *cis*-urocanic acid (induced by UV-B exposure; Figure 13, step 1), mainly by **A1**. This prevents the release of TNF- α , histamine, and PGE₂ [12].

- (iii.) Inhibiting PAF-R-mediated immunosuppression triggered by PAF-like lipid ligands. UV-induced membrane lipid oxidation (Figure 13, step 2) generates PAF-like lipid ligands (Figure 13, step 3) [12].
- (iv.) Disturbing IL-1 α/β signaling is mediated by inhibiting their heterodimer receptor, which includes IL-1R1, [13] mainly by A3. UV-induced ROS promote IL-1 β activation (Figure 13, step 5) [13].
- (v.) Disturbing EGF-R signaling is mediated by members of the A Disintegrin and A Metalloproteinase (ADAM) family [79]. UV-induced ROS activate some ADAM members (Figure 13, step 6) [79], which trigger EGF-R signaling (Figure 13, step 7) [80].

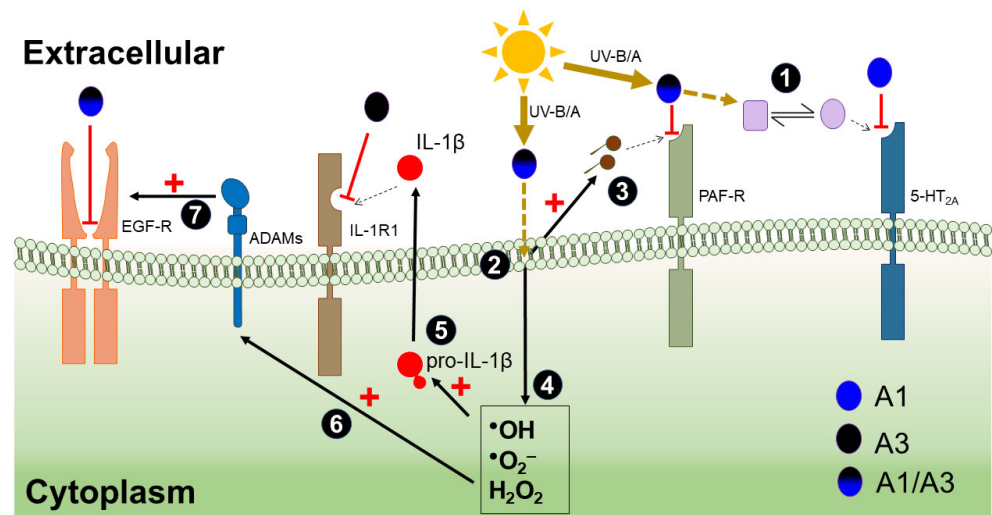


Figure 13. Proposed concomitant effects on UV-induced damage signaling by A1 and A3. The main UV-induced molecular events are summarized in seven steps, indicated by numbered black spheres: Step 1—UV-induced *cis*-urocanic acid isomerization. Step 2—UV-induced lipid peroxidation. Step 3—UV-induced generation of PAF-like lipid ligands. Step 4—UV-induced ROS generation. Step 5—ROS-mediated activation of pro-IL-1 β . Step 6—ROS-mediated activation of ADAMs. Step 7—Activation of EGF-R signaling by ADAMs.

Finally, it is fundamental to note that the experimental evaluation of the results found represents important challenges that were not addressed in this study. First, it is difficult to find a single model that cost effectively presents the possibility of assaying the targets evaluated here, and we know that high levels of cell surface expression of each protein are required for monitoring, which would imply building a model for each target. Second, it is challenging to obtain the quantities required to perform the analyses. However, the sustained consistency when compared to reference UV filters supports the rigor with which the *in silico* analyses were performed. Additionally, this work is the first to combine different mechanisms that may contribute to the orthogonal control of photodamage. These considerations are important in the design of future studies.

5. Conclusions

In this study, 34 uncovered *Streptomyces*-derived compounds that, besides meeting safety features for topically applied agents, also exhibited high *in silico* affinities, targeting multiple cellular receptors involved in UV-induced skin damage. Among these metabolites, aspergilazine A and phaeochromycin F displayed the best binding scores with the highest number of targets (i.e., 5-HT_{2A}, PAF-R, IL-1R1, and EGF-R), and their complexes evolved adequately over the time to reach stabilization after 30 ns. Therefore, they can be further explored to formulate skin photoprotection products, even as enhancers of the properties offered by some of the AUVFs. Additionally, considering the feasibility of *Streptomyces* strains

for biotechnological production of these compounds, our findings provide the opportunity to find a sustainable source of metabolites possessing photoprotective capabilities.

Supplementary Materials: The following supporting information can be downloaded at: <https://www.mdpi.com/article/10.3390/scipharm90030048/s1>, Table S1: Clustering of the 1981 selected compounds by *Flexphore* descriptor.

Author Contributions: Conceptualization, J.S.-S. and E.C.-B.; methodology, J.S.-S. and E.C.-B.; software, J.S.-S. and E.C.-B.; validation, J.S.-S. and E.C.-B.; formal analysis, J.S.-S. and E.C.-B.; investigation, J.S.-S.; resources, L.V., E.C.-B. and L.D.; data curation, J.S.-S. and E.C.-B.; writing—original draft preparation, J.S.-S.; writing—review and editing, L.V., E.C.-B. and L.D.; visualization, J.S.-S. and E.C.-B.; supervision, L.V. and L.D.; project administration, L.V. and L.D.; funding acquisition, L.V. and L.D. All authors have read and agreed to the published version of the manuscript.

Funding: This work was funded by Minciencias (Ministerio de Ciencia, Tecnología e Innovación), Colombia [project code 123080864187, contract 80740-168-2019] and Universidad de La Sabana [General Research Directorate, project ING-175-2016].

Data Availability Statement: The data used to support the findings of this study are provided within this article. However, any required further information can be provided by the corresponding author upon request.

Acknowledgments: Thanks to the Department of Norte de Santander (Colombia) for the JSS Ph.D. scholarship funding through the Minciencias Bicentenario grant. In addition, we thank Universidad Militar Nueva Granada for the financial support (project IMP-CIAS-2924) and Universidad de La Sabana for supporting the proofreading service.

Conflicts of Interest: The authors declare no conflict of interest.

References

1. Gilchrest, B.A. Actinic Injury. *Annu. Rev. Med.* **1990**, *41*, 199–210. [[CrossRef](#)]
2. Moan, J.; Grigalavicius, M.; Baturaite, Z.; Dahlback, A.; Juzeniene, A. The relationship between UV exposure and incidence of skin cancer. *Photodermatol. Photoimmunol. Photomed.* **2015**, *31*, 26–35. [[CrossRef](#)] [[PubMed](#)]
3. Martens, M.C.; Seebode, C.; Lehmann, J.; Emmert, S. Photocarcinogenesis and Skin Cancer Prevention Strategies: An Update. *Anticancer Res.* **2018**, *38*, 1153–1158. [[CrossRef](#)] [[PubMed](#)]
4. Lim, H.W.; Arellano-Mendoza, M.I.; Stengel, F. Current challenges in photoprotection. *J. Am. Acad. Dermatol.* **2017**, *76*, S91–S99. [[CrossRef](#)] [[PubMed](#)]
5. Paiva, J.P.; Diniz, R.R.; Leitão, A.C.; Cabral, L.M.; Fortunato, R.S.; Santos, B.A.M.C.; de Pádula, M. Insights and controversies on sunscreen safety. *Crit. Rev. Toxicol.* **2020**, *50*, 707–723. [[CrossRef](#)]
6. Schaap, I.; Slijkerman, D.M.E. An environmental risk assessment of three organic UV-filters at Lac Bay, Bonaire, Southern Caribbean. *Mar. Pollut. Bull.* **2018**, *135*, 490–495. [[CrossRef](#)]
7. Kaiser, D.; Sieratowicz, A.; Zielke, H.; Oetken, M.; Hollert, H.; Oehlmann, J. Ecotoxicological effect characterisation of widely used organic UV filters. *Environ. Pollut.* **2012**, *163*, 84–90. [[CrossRef](#)]
8. Tsui, M.M.P.; Leung, H.W.; Wai, T.C.; Yamashita, N.; Taniyasu, S.; Liu, W.; Lam, P.K.S.; Murphy, M.B. Occurrence, distribution and ecological risk assessment of multiple classes of UV filters in surface waters from different countries. *Water Res.* **2014**, *67*, 55–65. [[CrossRef](#)]
9. Tsui, M.M.P.; Lam, J.C.W.; Ng, T.Y.; Ang, P.O.; Murphy, M.B.; Lam, P.K.S. Occurrence, Distribution, and Fate of Organic UV Filters in Coral Communities. *Environ. Sci. Technol.* **2017**, *51*, 4182–4190. [[CrossRef](#)]
10. Lozano, C.; Givens, J.; Stien, D.; Matallana-Surget, S.; Lebaron, P. Bioaccumulation and Toxicological Effects of UV-Filters on Marine Species. In *Sunscreens in Coastal Ecosystems*; Springer International Publishing: Cham, Switzerland, 2020; pp. 85–130.
11. Poon, F.; Kang, S.; Chien, A.L. Mechanisms and treatments of photoaging. *Photodermatol. Photoimmunol. Photomed.* **2015**, *31*, 65–74. [[CrossRef](#)]
12. Bernard, J.J.; Gallo, R.L.; Krutmann, J. Photoimmunology: How ultraviolet radiation affects the immune system. *Nat. Rev. Immunol.* **2019**, *19*, 688–701. [[CrossRef](#)] [[PubMed](#)]
13. Nasti, T.H.; Timares, L. Inflammasome activation of IL-1 family mediators in response to cutaneous photodamage. *Photochem. Photobiol.* **2012**, *88*, 1111–1125. [[CrossRef](#)] [[PubMed](#)]
14. Muthusamy, V.; Piva, T.J. The UV response of the skin: A review of the MAPK, NFκB and TNFα signal transduction pathways. *Arch. Dermatol. Res.* **2010**, *302*, 5–17. [[CrossRef](#)] [[PubMed](#)]
15. El-Abaseri, T.B.; Hansen, L.A. EGFR Activation and Ultraviolet Light-Induced Skin Carcinogenesis. *J. Biomed. Biotechnol.* **2007**, *2007*, 1–4. [[CrossRef](#)]

16. Rundhaug, J.E.; Mikulec, C.; Pavone, A.; Fischer, S.M. A role for cyclooxygenase-2 in ultraviolet light-induced skin carcinogenesis. *Mol. Carcinog.* **2007**, *46*, 692–698. [[CrossRef](#)]
17. Pinnell, S.R. Cutaneous photodamage, oxidative stress, and topical antioxidant protection. *J. Am. Acad. Dermatol.* **2003**, *48*, 1–22. [[CrossRef](#)]
18. Nichols, J.A.; Katiyar, S.K. Skin photoprotection by natural polyphenols: Anti-inflammatory, antioxidant and DNA repair mechanisms. *Arch. Dermatol. Res.* **2010**, *302*, 71–83. [[CrossRef](#)]
19. Shaath, N.A. Ultraviolet filters. *Photochem. Photobiol. Sci.* **2010**, *9*, 464. [[CrossRef](#)]
20. Shaath, N.A. The Chemistry of Ultraviolet Filters. In *Principles and Practice of Photoprotection*; Springer International Publishing: Cham, Switzerland, 2016; pp. 143–157. ISBN 9783319293820.
21. Subhadarshani, S.; Athar, M.; Elmets, C.A. Photocarcinogenesis. *Curr. Dermatol. Rep.* **2020**, *9*, 189–199. [[CrossRef](#)]
22. Giacomoni, P.U. Appropriate Technologies to Accompany Sunscreens in the Battle Against Ultraviolet, Superoxide, and Singlet Oxygen. *Antioxidants* **2020**, *9*, 1091. [[CrossRef](#)]
23. Romanhole, R.C.; Fava, A.L.M.; Tundisi, L.L.; de Macedo, L.M.; dos Santos, É.M.; Ataide, J.A.; Mazzola, P.G. Unplanned absorption of sunscreen ingredients: Impact of formulation and evaluation methods. *Int. J. Pharm.* **2020**, *591*, 120013. [[CrossRef](#)]
24. Oral, D.; Yirun, A.; Erkekoglu, P. Safety Concerns of Organic Ultraviolet Filters: Special Focus on Endocrine-Disrupting Properties. *J. Environ. Pathol. Toxicol. Oncol.* **2020**, *39*, 201–212. [[CrossRef](#)]
25. Koehn, F.E.; Carter, G.T. The evolving role of natural products in drug discovery. *Nat. Rev. Drug Discov.* **2005**, *4*, 206–220. [[CrossRef](#)]
26. Lin, B.; Tao, Y. Whole-cell biocatalysts by design. *Microb. Cell Fact.* **2017**, *16*, 106. [[CrossRef](#)] [[PubMed](#)]
27. Belknap, K.C.; Park, C.J.; Barth, B.M.; Andam, C.P. Genome mining of biosynthetic and chemotherapeutic gene clusters in *Streptomyces* bacteria. *Sci. Rep.* **2020**, *10*, 2003. [[CrossRef](#)] [[PubMed](#)]
28. Sánchez-Suárez, J.; Coy-Barrera, E.; Villamil, L.; Díaz, L. *Streptomyces*-Derived Metabolites with Potential Photoprotective Properties—A Systematic Literature Review and Meta-Analysis on the Reported Chemodiversity. *Molecules* **2020**, *25*, 3221. [[CrossRef](#)]
29. Sliwoski, G.; Kothiwale, S.; Meiler, J.; Lowe, E.W. Computational Methods in Drug Discovery. *Pharmacol. Rev.* **2014**, *66*, 334–395. [[CrossRef](#)]
30. Brogi, S.; Ramalho, T.C.; Kuca, K.; Medina-Franco, J.L.; Valko, M. Editorial: In silico Methods for Drug Design and Discovery. *Front. Chem.* **2020**, *8*, 612. [[CrossRef](#)] [[PubMed](#)]
31. Phatak, S.S.; Stephan, C.C.; Cavasotto, C.N. High-throughput and in silico screenings in drug discovery. *Expert Opin. Drug Discov.* **2009**, *4*, 947–959. [[CrossRef](#)] [[PubMed](#)]
32. Bolognesi, M.L.; Cavalli, A. Multitarget Drug Discovery and Polypharmacology. *ChemMedChem* **2016**, *11*, 1190–1192. [[CrossRef](#)] [[PubMed](#)]
33. Anighoro, A.; Bajorath, J.; Rastelli, G. Polypharmacology: Challenges and Opportunities in Drug Discovery. *J. Med. Chem.* **2014**, *57*, 7874–7887. [[CrossRef](#)] [[PubMed](#)]
34. Kitchen, D.B.; Decornez, H.; Furr, J.R.; Bajorath, J. Docking and scoring in virtual screening for drug discovery: Methods and applications. *Nat. Rev. Drug Discov.* **2004**, *3*, 935–949. [[CrossRef](#)] [[PubMed](#)]
35. Pinzi, L.; Rastelli, G. Molecular Docking: Shifting Paradigms in Drug Discovery. *Int. J. Mol. Sci.* **2019**, *20*, 4331. [[CrossRef](#)]
36. Elokely, K.M.; Doerken, R.J. Docking Challenge: Protein Sampling and Molecular Docking Performance. *J. Chem. Inf. Model.* **2013**, *53*, 1934–1945. [[CrossRef](#)]
37. Yuriev, E.; Ramsland, P.A. Latest developments in molecular docking: 2010–2011 in review. *J. Mol. Recognit.* **2013**, *26*, 215–239. [[CrossRef](#)]
38. Salmaso, V.; Moro, S. Bridging molecular docking to molecular dynamics in exploring ligand-protein recognition process: An overview. *Front. Pharmacol.* **2018**, *9*, 923. [[CrossRef](#)]
39. Moumbock, A.F.A.; Gao, M.; Qaseem, A.; Li, J.; Kirchner, P.A.; Ndingkokhar, B.; Bekono, B.D.; Simoben, C.V.; Babiaka, S.B.; Malange, Y.I.; et al. StreptomeDB 3.0: An updated compendium of streptomycetes natural products. *Nucleic Acids Res.* **2021**, *49*, D600–D604. [[CrossRef](#)] [[PubMed](#)]
40. Krämer, M.; Sachsenmaier, C.; Herrlich, P.; Rahmsdorf, H.J. UV irradiation-induced interleukin-1 and basic fibroblast growth factor synthesis and release mediate part of the UV response. *J. Biol. Chem.* **1993**, *268*, 6734–6741. [[CrossRef](#)]
41. Sander, T.; Freyss, J.; Von Korff, M.; Rufener, C. DataWarrior: An open-source program for chemistry aware data visualization and analysis. *J. Chem. Inf. Model.* **2015**, *55*, 460–473. [[CrossRef](#)]
42. Trott, O.; Olson, A.J. AutoDock Vina: Improving the speed and accuracy of docking with a new scoring function, efficient optimization, and multithreading. *J. Comput. Chem.* **2009**, *31*, 455–461. [[CrossRef](#)]
43. Yang, C.Y. Identification of potential small molecule allosteric modulator sites on IL-1R1 ectodomain using accelerated conformational sampling method. *PLoS ONE* **2015**, *10*, e0118671. [[CrossRef](#)]
44. Yang, R.Y.C.; Yang, K.S.; Pike, L.J.; Marshall, G.R. Targeting the dimerization of epidermal growth factor receptors with small-molecule inhibitors. *Chem. Biol. Drug Des.* **2010**, *76*, 1–9. [[CrossRef](#)]
45. Cossi, M.; Rega, N.; Scalmani, G.; Barone, V. Energies, structures, and electronic properties of molecules in solution with the C-PCM solvation model. *J. Comput. Chem.* **2003**, *24*, 669–681. [[CrossRef](#)]

46. Krieger, E.; Vriend, G. New ways to boost molecular dynamics simulations. *J. Comput. Chem.* **2015**, *36*, 996–1007. [[CrossRef](#)] [[PubMed](#)]
47. Kumari, R.; Kumar, R.; Lynn, A. g_mmpbsa—A GROMACS Tool for High-Throughput MM-PBSA Calculations. *J. Chem. Inf. Model.* **2014**, *54*, 1951–1962. [[CrossRef](#)] [[PubMed](#)]
48. Heberle, H.; Meirelles, G.V.; da Silva, F.R.; Telles, G.P.; Minghim, R. InteractiVenn: A web-based tool for the analysis of sets through Venn diagrams. *BMC Bioinform.* **2015**, *16*, 169. [[CrossRef](#)] [[PubMed](#)]
49. Nohynek, G.J.; Schaefer, H. Benefit and risk of organic ultraviolet filters. *Regul. Toxicol. Pharmacol.* **2001**, *33*, 285–299. [[CrossRef](#)] [[PubMed](#)]
50. Magnusson, B.M.; Pugh, W.J.; Roberts, M.S. Simple rules defining the potential of compounds for transdermal delivery or toxicity. *Pharm. Res.* **2004**, *21*, 1047–1054. [[CrossRef](#)]
51. Hevener, K.E.; Zhao, W.; Ball, D.M.; Babaoglu, K.; Qi, J.; White, S.W.; Lee, R.E. Validation of Molecular Docking Programs for Virtual Screening against Dihydropteroate Synthase. *J. Chem. Inf. Model.* **2009**, *49*, 444–460. [[CrossRef](#)] [[PubMed](#)]
52. Couteau, C.; Chauvet, C.; Papisaris, E.; Coiffard, L. UV Filters, Ingredients with a Recognized Anti-Inflammatory Effect. *PLoS ONE* **2012**, *7*, e46187. [[CrossRef](#)]
53. Dougherty, D.A. The Cation– π Interaction. *Acc. Chem. Res.* **2013**, *46*, 885–893. [[CrossRef](#)] [[PubMed](#)]
54. Petukhov, M.; Uegaki, K.; Yumoto, N.; Yoshikawa, S.; Serrano, L. Position dependence of amino acid intrinsic helical propensities II: Non-charged polar residues: Ser, Thr, Asn, and Gln. *Protein Sci.* **1999**, *8*, 2144–2150. [[CrossRef](#)] [[PubMed](#)]
55. Cochran, D.A.E.; Doig, A.J. Effect of the N2 residue on the stability of the α -helix for all 20 amino acids. *Protein Sci.* **2008**, *10*, 1305–1311. [[CrossRef](#)] [[PubMed](#)]
56. Raffa, R.B.; Pergolizzi, J.V.; Taylor, R.; Kitzen, J.M. Sunscreen bans: Coral reefs and skin cancer. *J. Clin. Pharm. Ther.* **2019**, *44*, 134–139. [[CrossRef](#)] [[PubMed](#)]
57. Springsteen, A.; Yurek, R.; Frazier, M.; Carr, K.F. In vitro measurement of sun protection factor of sunscreens by diffuse transmittance. *Anal. Chim. Acta* **1999**, *380*, 155–164. [[CrossRef](#)]
58. Srivastava, P.; Tiwari, A. Critical Role of Computer Simulations in Drug Discovery and Development. *Curr. Top. Med. Chem.* **2017**, *17*, 2422–2432. [[CrossRef](#)]
59. Atanasov, A.G.; Zotchev, S.B.; Dirsch, V.M.; Orhan, I.E.; Banach, M.; Rollinger, J.M.; Barreca, D.; Weckwerth, W.; Bauer, R.; Bayer, E.A.; et al. Natural products in drug discovery: Advances and opportunities. *Nat. Rev. Drug Discov.* **2021**, *20*, 200–216. [[CrossRef](#)]
60. Korkina, L.G. Current Trends in Medicinal Chemistry of Photoprotection and Phototherapy. *Curr. Med. Chem.* **2018**, *25*, 5466–5468. [[CrossRef](#)]
61. Dickinson, S.E.; Wondrak, G.T. TLR4-directed Molecular Strategies Targeting Skin Photodamage and Carcinogenesis. *Curr. Med. Chem.* **2019**, *25*, 5487–5502. [[CrossRef](#)]
62. Tadano, S.; Sugimachi, Y.; Sumimoto, M.; Tsukamoto, S.; Ishikawa, H. Collective Synthesis and Biological Evaluation of Tryptophan-Based Dimeric Diketopiperazine Alkaloids. *Chem.-Eur. J.* **2016**, *22*, 1277–1291. [[CrossRef](#)]
63. Li, J.; Lu, C.-H.; Zhao, B.-B.; Zheng, Z.-H.; Shen, Y.-M. Phaeochromycins F–H, three new polyketide metabolites from *Streptomyces* sp. DSS-18. *Beilstein J. Org. Chem.* **2008**, *4*, 46. [[CrossRef](#)] [[PubMed](#)]
64. Wang, J.N.; Zhang, H.J.; Li, J.Q.; Ding, W.J.; Ma, Z.J. Bioactive Indolocarbazoles from the Marine-Derived *Streptomyces* sp. DT-A61. *J. Nat. Prod.* **2018**, *81*, 949–956. [[CrossRef](#)]
65. Rab, E.; Kekos, D.; Roussis, V.; Ioannou, E. α -Pyrone Polyketides from *Streptomyces ambofaciens* BI0048, an Endophytic Actinobacterial Strain Isolated from the Red Alga *Laurencia glandulifera*. *Mar. Drugs* **2017**, *15*, 389. [[CrossRef](#)]
66. Seebode, C.; Lehmann, J.; Emmert, S. Photocarcinogenesis and Skin Cancer Prevention Strategies. *Anticancer Res.* **2016**, *36*, 1371–1378. [[PubMed](#)]
67. Liu, J.; Gu, B.; Yang, L.; Yang, F.; Lin, H. New Anti-inflammatory Cyclopeptides From a Sponge-Derived Fungus *Aspergillus violaceofuscus*. *Front. Chem.* **2018**, *6*, 226. [[CrossRef](#)] [[PubMed](#)]
68. Wen, H.; Liu, X.; Zhang, Q.; Deng, Y.; Zang, Y.; Wang, J.; Liu, J.; Zhou, Q.; Hu, L.; Zhu, H.; et al. Three New Indole Diketopiperazine Alkaloids from *Aspergillus ochraceus*. *Chem. Biodivers.* **2018**, *15*, e1700550. [[CrossRef](#)] [[PubMed](#)]
69. Bulger, E.M.; Arbabi, S.; Garcia, I.; Maier, R.V. The macrophage response to endotoxin requires platelet activating factor. *Shock* **2002**, *17*, 173–179. [[CrossRef](#)]
70. Im, S.Y.; Han, S.J.; Ko, H.M.; Choi, J.H.; Chun, S.B.; Lee, D.G.; Ha, T.Y.; Lee, H.-K. Involvement of nuclear factor- κ B in platelet-activating factor-mediated tumor necrosis factor- α expression. *Eur. J. Immunol.* **1997**, *27*, 2800–2804. [[CrossRef](#)]
71. Liu, Q.; Mu, Y.; An, Q.; Xun, J.; Ma, J.; Wu, W.; Xu, M.; Xu, J.; Han, L.; Huang, X. Total synthesis and anti-inflammatory evaluation of violacin A and its analogues. *Bioorg. Chem.* **2020**, *94*, 103420. [[CrossRef](#)]
72. Graziani, E.I.; Ritacco, F.V.; Bernan, V.S.; Telliez, J.-B. Phaeochromycins A–E, Anti-inflammatory Polyketides Isolated from the Soil Actinomycete *Streptomyces* p haeochromogenes LL-P018. *J. Nat. Prod.* **2005**, *68*, 1262–1265. [[CrossRef](#)]
73. Kimura, K.T.; Asada, H.; Inoue, A.; Kadji, F.M.N.; Im, D.; Mori, C.; Arakawa, T.; Hirata, K.; Nomura, Y.; Nomura, N.; et al. Structures of the 5-HT_{2A} receptor in complex with the antipsychotics risperidone and zotepine. *Nat. Struct. Mol. Biol.* **2019**, *26*, 121–128. [[CrossRef](#)] [[PubMed](#)]
74. Yarden, Y.; Sliwkowski, M.X. Untangling the ErbB signalling network. *Nat. Rev. Mol. Cell Biol.* **2001**, *2*, 127–137. [[CrossRef](#)] [[PubMed](#)]

75. Arkin, M.M.R.; Wells, J.A. Small-molecule inhibitors of protein-protein interactions: Progressing towards the dream. *Nat. Rev. Drug Discov.* **2004**, *3*, 301–317. [[CrossRef](#)]
76. Acuner Ozbabacan, S.E.; Gursoy, A.; Nussinov, R.; Keskin, O. The Structural Pathway of Interleukin 1 (IL-1) Initiated Signaling Reveals Mechanisms of Oncogenic Mutations and SNPs in Inflammation and Cancer. *PLoS Comput. Biol.* **2014**, *10*, e1003470. [[CrossRef](#)]
77. Ogiso, H.; Ishitani, R.; Nureki, O.; Fukai, S.; Yamanaka, M.; Kim, J.H.; Saito, K.; Sakamoto, A.; Inoue, M.; Shirouzu, M.; et al. Crystal structure of the complex of human epidermal growth factor and receptor extracellular domains. *Cell* **2002**, *110*, 775–787. [[CrossRef](#)]
78. Walker, F.; Orchard, S.G.; Jorissen, R.N.; Hall, N.E.; Zhang, H.-H.; Hoyne, P.A.; Adams, T.E.; Johns, T.G.; Ward, C.; Garrett, T.P.J.; et al. CR1/CR2 Interactions Modulate the Functions of the Cell Surface Epidermal Growth Factor Receptor. *J. Biol. Chem.* **2004**, *279*, 22387–22398. [[CrossRef](#)] [[PubMed](#)]
79. Kataoka, H. EGFR ligands and their signaling scissors, ADAMs, as new molecular targets for anticancer treatments. *J. Dermatol. Sci.* **2009**, *56*, 148–153. [[CrossRef](#)]
80. Singh, B.; Schneider, M.; Knyazev, P.; Ullrich, A. UV-induced EGFR signal transactivation is dependent on proligand shedding by activated metalloproteases in skin cancer cell lines. *Int. J. Cancer* **2009**, *124*, 531–539. [[CrossRef](#)] [[PubMed](#)]